Review of Scientific Instruments

3D printed spherical environmental chamber for neutron reflectometry and grazing-incidence small-angle neutron scattering experiments

Cite as: Rev. Sci. Instrum. **91**, 113903 (2020); https://doi.org/10.1063/5.0012652
Submitted: 03 May 2020 . Accepted: 18 October 2020 . Published Online: 04 November 2020

Tobias Widmann, Lucas P. Kreuzer, Gaetano Mangiapia, Martin Haese, Henrich Frielinghaus, and Peter Müller-Buschbaum

AIP Publishing

Review of Scientific Instruments ARTICLE scitation.org/journal/rsi

3D printed spherical environmental chamber for neutron reflectometry and grazing-incidence small-angle neutron scattering experiments

Cite as: Rev. Sci. Instrum. 91, 113903 (2020); doi: 10.1063/5.0012652
Submitted: 3 May 2020 • Accepted: 18 October 2020 •
Published Online: 4 November 2020

Tobias Widmann,[1] Lucas P. Kreuzer,[1] Gaetano Mangiapia,[2] Martin Haese,[2] Henrich Frielinghaus,[3] and Peter Müller-Buschbaum[1,4,a)]

AFFILIATIONS

[1] Lehrstuhl für Funktionelle Materialien, Physik Department, Technische Universität München, James-Franck-Str. 1, 85748 Garching, Germany
[2] German Engineering Materials Science Center (GEMS) at Heinz Maier-Leibnitz Zentrum (MLZ), Helmholtz-Zentrum Geesthacht GmbH, Lichtenbergstr. 1, 85748 Garching, Germany
[3] Jülich Centre for Neutron Science at Heinz Maier-Leibnitz Zentrum, Lichtenbergstr. 1, 85748 Garching, Germany
[4] Heinz Maier-Leibnitz Zentrum (MLZ), Technische Universität München, Lichtenbergstr. 1, 85748 Garching, Germany

[a)] **Author to whom correspondence should be addressed:** muellerb@ph.tum.de

ABSTRACT

In neutron scattering on soft matter, an important concern is the control and stability of environmental conditions surrounding the sample. Complex sample environment setups are often expensive to fabricate or simply not achievable by conventional workshop manufacturing. We make use of state-of-the-art 3D metal-printing technology to realize a sample environment for large sample sizes, optimized for investigations on thin film samples with neutron reflectometry (NR) and grazing-incidence small-angle neutron scattering (GISANS). With the flexibility and freedom of design given by 3D metal-printing, a spherical chamber with fluidic channels inside its walls is printed from an AlSi10Mg powder via selective laser melting (SLM). The thin channels ensure a homogeneous heating of the sample environment from all directions and allow for quick temperature switches in well-equilibrated atmospheres. In order to optimize the channel layout, flow simulations were carried out and verified in temperature switching tests. The spherical, edgeless design aids the prevention of condensation inside the chamber in case of high humidity conditions. The large volume of the sample chamber allows for high flexibility in sample size and geometry. While a small-angle neutron scattering (SANS) measurement through the chamber walls reveals a strong isotropic scattering signal resulting from the evenly orientated granular structure introduced by SLM, a second SANS measurement through the windows shows no additional background originating from the chamber. Exemplary GISANS and NR measurements in time-of-flight mode are shown to prove that the chamber provides a stable, background free sample environment for the investigation of thin films.

I. INTRODUCTION

The use of high flux neutron beams offers unique investigation methods to gather more insight into the structure and dynamics of inorganic and organic matter. Compared to x-ray scattering, where the scattering cross section increases with an increasing atomic number of the probed atom, neutron scattering lengths differ largely by the element and isotope, independent of the atomic number.[1] Thus, especially for studying biological and soft matter samples, which foremost involve light elements such as hydrogen, carbon, nitrogen, and oxygen (elements with very similar x-ray scattering lengths), neutron scattering can provide a good contrast.[2] The contrast between hydrogen ($SLD_{H_2O} = -0.559 \times 10^{-6}$ Å^{-2}) and its isotope deuterium ($SLD_{D_2O} = 6.36 \times 10^{-6}$ Å^{-2}) is of particular benefit.[3] By using deuterated samples and solvents, contrast matching or enhancement of different constituents of the samples can be achieved to improve the quality of the neutron scattering data.

Neutron reflectometry (NR)[4–6] and grazing-incidence small-angle neutron scattering (GISANS),[7–9] at a normal fixed wavelength or in time-of-flight (ToF) mode, are two advanced scattering techniques that allow the investigation of the vertical and lateral structures of soft matter thin-film samples.[10] Due to the large surface-to-volume ratio and the confinement against a solid support, the organic materials often exhibit uniquely different physical properties compared to their bulk states or enable new functionality. Therefore, NR and GISANS serve a broad field of scientific interest in soft matter research, such as in photovoltaics,[11–14] electrodes,[15,16] light emitting diodes,[17,18] catalysts,[19] sensors,[20] surface coatings,[21–23] and interfaces.[24–27] A common feature of soft matter samples is their high sensitivity to thermodynamic conditions of their surroundings. Often, even with only slight changes in the ambient temperature, humidity or pressure can lead to a strong response in one or more of their physical properties.[28,29] For this reason, a stable and controllable environment for the probed samples is a necessity. Consequently, neutron experimentation is closely related to the production and provision of suitable sample environments for allocated experiments.[30] There already exist a variety of such environments with well-controlled thermodynamic conditions, including different kinds of humidity chambers and cells.[31–33] However, these are usually manufactured of high purity aluminum alloys via subtractive manufacturing. Parts are produced by cutting material from solid blocks in multiple steps before being assembled to the final product. This requires a lot of time, work force, and material. Moreover, subtractive manufacturing is limited by what workshops are able to fabricate, i.e., their knowhow and their machining equipment. In contrast, 3D printing is an additive production process where a product is built layer-by-layer in a single step process from an initial 3D design. This approach requires less man power, produces less waste material, and, at least for complex objects, has shorter production times.[34] Thus, the total production costs can be reduced compared to subtractive manufacturing. In the industry, 3D printing technology is already a well-established routine for prototyping, customization, and production.[35] Moreover, it is also of high interest for a custom-oriented field such as sample environments for neutron experimentation as it allows for the fabrication of highly complex and specialized designs. It was already used to produce shielding materials for neutron beamlines.[36,37]

Various 3D printing techniques are specific to different materials and can use filaments, powders, or liquids as base materials. For the production of metal parts, established techniques are Direct Metal Laser Sintering (DMLS), Selective Laser Melting (SLM), or Electron Beam Melting (EBM).[38] A metal powder bed is heated locally to high temperatures until the granules start fusing together (DMLS) or, using even higher energies, until they are completely molten (SLM, EBM). Complete melting of the powder results in a more homogeneous part with lower porosity and provides better control over its crystal structure.

In this work, we report on the design of a spherical environmental chamber with a fluid channel system integrated into its walls for optimized heat distribution, which is fabricated in an additive manufacturing process via SLM. The chamber is designed for stable environmental sample conditions during NR and GISANS experiments on thin films. The granularity of the 3D printed chamber is investigated with small-angle neutron scattering (SANS). The heat distribution and buildup inside the environmental chamber is simulated by flow simulation and investigated in temperature switching experiments. Finally, exemplary ToF-NR and ToF-GISANS measurements are carried out on a partially deuterated diblock-copolymer thin film, as well as a metal-coated microgel thin film, to demonstrate the performance of the chamber in real neutron scattering experiments.[39]

II. ENVIRONMENTAL CHAMBER DESIGN AND PRINT

The design of the environmental chamber is shown in Fig. 1. Foremost, it aims at stable and controllable thermodynamic conditions while retaining enough flexibility to cover a large field of experiment-related interests, such as complementary spectral reflectance measurements,[40] four-point measurements,[41] I–V characterization,[42] different trigger methods such as light irradiation or humidity,[43,44] different sample sizes, and vertical or horizontal sample alignment. Since edges and corners are critical points for a stable temperature and humidity, a spherical design was chosen.[45] It allows experiments with high humidity inside the chamber, as condensation is strongly reduced within an edgeless design. The wireframe model shown in Fig. 1(a) gives a side view of the chamber and labels its dimensions in mm. The aimed maximum sample size of 70

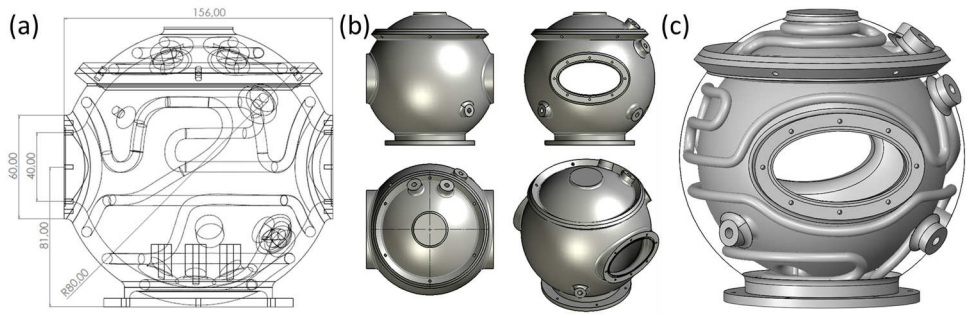

FIG. 1. (a) Wireframe model of the environmental chamber in side view. The neutron beam enters through the left window and exits through the right one. The labels denote the chamber measures in mm. (b) The chamber viewed from the side (top left), the front (top right), the top (bottom left), and isometric (bottom right). (c) 3D visualization of the fluid channels embedded in the chamber walls. They have a diameter of 6 mm and are centered within the 10 mm thick walls. The inner gray sphere shows the inner chamber wall, and the outer black circle indicates the outer wall position.

× 70 mm^2 was deciding for the overall chamber size. Generally, larger samples allow for better statistics and can drastically reduce measurement times. However, environmental stability, especially closely around the samples, needs to be considered. The environmental chamber has an inner diameter of 140 mm and provides a relatively large volume of 1.4 l, which allocates rectangular samples up to a size of 70 × 70 mm^2 with at least 15 mm distance to the chamber walls to reduce edge effects upon rapid temperature changes in the chamber. Moreover, there is enough room for additional measurement equipment if necessary (e.g., sensors, complementary measurement techniques, and additional experimental equipment). The chambers windows, visible in the different viewpoints in Fig. 1(b), are 156 mm apart from each other. The windows are elliptical to compromise between a large accessible scattering angle and heat losses causing a perturbed heat distribution. They have a height of 40 mm and a width of 90 mm and allow incident angles of up to 5° at a neutron beam height and width of 2 mm and 60 mm, respectively.

For temperature control, a refrigerated or heated fluid flows through a channel path within the chamber walls. The pathway is shown in the wireframe model in Fig. 1(a) and is also shown in a 3D visualization in Fig. 1(c) for better clarity. The fluid channels have a diameter of 6 mm and are centered within the 10 mm thick walls. Although the fluid channel walls are only 2 mm thick, the 3D printing technique is able to manufacture stable walls. The path length through the chamber base and lid is 2.4 m in total and provides enough time and surface area for a thorough heat transfer. In addition to the openings to the fluid channel, the chamber has additional holes that lead directly into the chamber to connect electronics, a gas-flow, or additional optional features.

The environmental chamber is printed via SLM (EOS M290, PROTIQ GmbH, Blomberg, Germany), which forms a powder bed of the aluminum alloy AlSi10Mg.[46] The chamber is built up layer by layer with a single layer thickness of 25 μm. The powder is fully melted and forms a dense and homogeneous bulk material. The construction chamber is flooded with an inert gas to prevent oxidation of the material during the printing process. After the printing, a heat treatment is applied to the chamber in order to form a stable intermetallic phase, which provides the aluminum alloy with a high and direction-independent tensile strength.[47] The printed chamber has a weight of 1.9 kg. It is shown in Fig. 2. Manufacturing time is less than 24 h, which allows for quick duplication or modification. The touching surfaces of the windows, the lid, and the connectors are polished afterward to ensure a gas tight sealing of the environmental chamber. In Fig. 2(a), the finished chamber with already installed connectors is shown. The golden brass hose nipples are the connectors for the heating or cooling fluid to the fluid channels inside the base and lid of the chamber. The blue compression fittings can be used to lead a gas-flow in and out of the chamber. The flange nipple visible on the lower left-hand side of the chamber is shrink-fitted into the chamber and used to connect electronics such as temperature and humidity sensors inside the chamber via interchangeable plugs. The chamber windows are covered with a 0.1 mm aluminum foil, which is clamped by two elliptical aluminum rings screwed against the chamber. It offers minimal attenuation of the neutron beam. All openings are sealed by polytetrafluoroethylene (PTFE) O-rings to ensure that there is no convection via air with the surrounding environment.

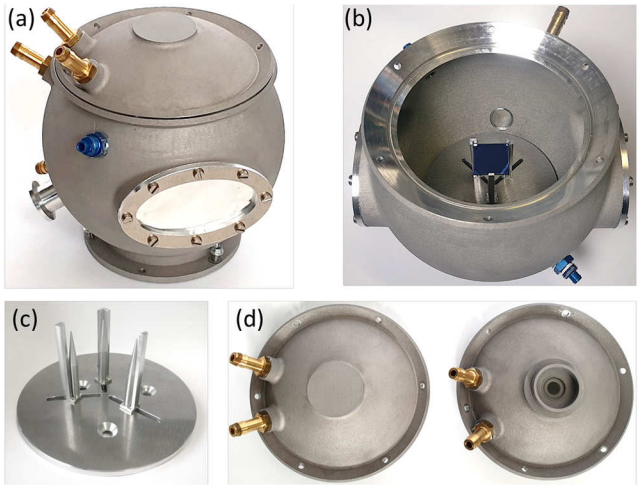

FIG. 2. (a) Photograph of the 3D printed sample chamber with connectors and aluminum foil windows. The golden hose nipples are connectors to the heating circuit, and the blue compression fittings can be used as in- and outlet for a gas flow. The flange nipple on the bottom left is used to connect to the electronics inside the chamber via a LEMO plug. (b) Interior view of the chamber where the sample holder and sample (blue square) are located. (c) Close-up view of the sample holder. (d) Top view showing the standard lid (left) and a lid with a calcium fluoride (CaF_2) glass for complementary spectral reflectance measurements (right).

The inside of the chamber hosts a base plate on which various setups can be installed. In Fig. 2(b), the inside of the chamber is shown. An adjustable sample holder with three aluminum pins is shown carrying a 20 × 20 mm^2 thin film sample with the sample surface aligned to the center of the chamber. The positions of the pins can be adjusted along the long holes in the baseplate to accommodate samples of different sizes from 10 × 10 mm^2 up to 70 × 70 mm^2 [see Fig. 2(c)]. Moreover, with the use of optional aluminum bars, the sample can be protected against sliding off the pins in the case of any physical chamber movement. The bars and pins are positioned in order to avoid background generation by the neutron beam. Additional measurement equipment can be installed via different lids, as suggested in Fig. 2(d), where the standard lid and a lid with a calcium fluoride (CaF_2) glass for complementary spectral reflectance measurements are shown. To ensure no condensation on the CaF_2 window during high humidity experiments, it is tightly fitted into a recess in the chamber lid together with a heat conducting paste. Additionally, the optics of the spectral reflectance setup will cover the opening to the CaF_2 window, creating an air pocket, which has the same temperature as that of the chamber.

III. CHAMBER CHARACTERIZATION

In order to estimate and optimize the temperature distribution and response within the chamber and its sample volume before the 3D printing, a heated and a cooled liquid flow through the chamber are simulated using the SolidWorks flow simulation software. The water's flow path is set to first circulate through the lid before entering at the bottom of the base and finally exiting at the top. In this

way, an even temperature distribution between the top and bottom of the chamber can be achieved. In the simulation, the heat transfer coefficient to the surroundings is set to 10 W m^{-2} K^{-1}, assuming a non-turbulent airflow around the chamber.

In the heating simulation, the initial chamber temperature is set to a room temperature of 20 °C. We assume a water flow heated to 50 °C entering the fluid channels with a flowrate of 30 ml s^{-1}, which corresponds to a flow rate of 1.1 m s^{-1} for a channel diameter of 6 mm. The results of the simulation are shown in Fig. 3.

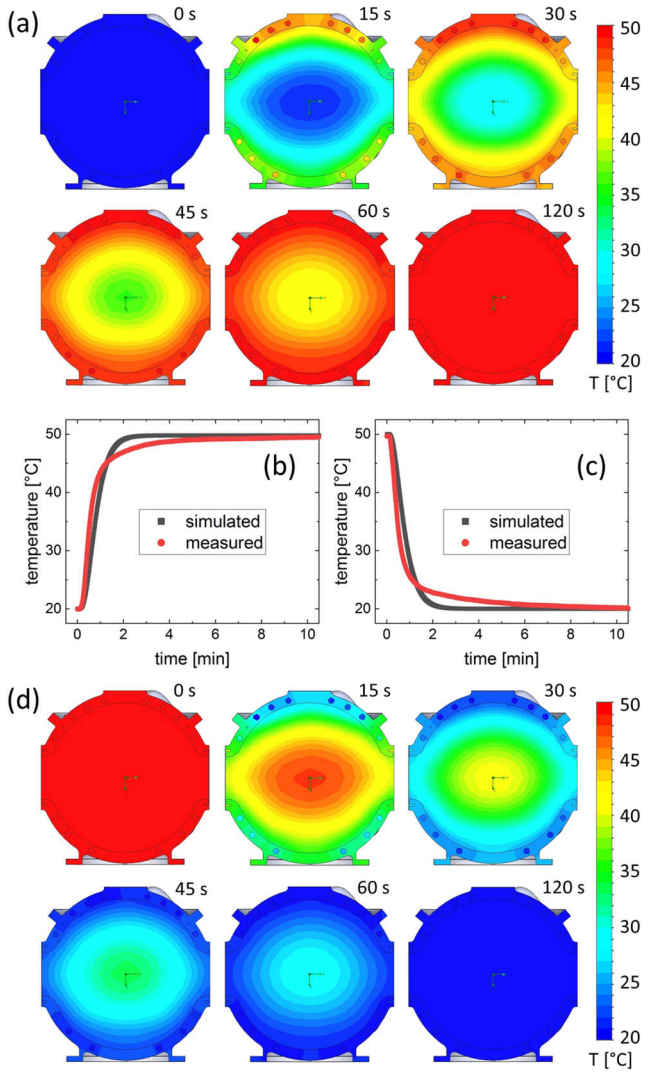

FIG. 3. (a) Sectional views of the chamber during a heating simulation over a period of 2 min. Each color in the contour plots corresponds to an isothermal range of 1 °C. (b) Temperature at the center of the chamber during the heating from 20 °C to 50 °C, obtained from the flow simulation (black) and the laboratory experiment (red). (c) Temperature at the center of the chamber during the cooling from 50 °C to 20 °C obtained from the flow simulation (black) and the laboratory experiment (red). (d) Sectional views of the chamber during the cooling simulation over a period of 2 min.

The sectional views in Fig. 3(a) depict the central cross section of the chamber and its air volume perpendicular to the windows. The temperature is shown as a contour color plot, with each individual color corresponding to an isothermal range of 1 °C. In the simulation, the chamber is heated from 20 °C to 50 °C within 2 min. The isotherms show that the temperature develops in an elliptical pattern around the center of the chamber where the sample is located. In order to validate these simulations, a thermal jump experiment is performed with the 3D printed chamber. The initial temperature of the chamber is kept at 20 °C by a refrigerated heating circulator (FP50-HL, JULABO Labortechnik GmbH, Seelbach, Germany), which is subsequently substituted by an identical heating circulator, preset to 50 °C. The temperature is measured at the center of the chamber with a combined humidity and temperature sensor (SHT3x, Sensirion AG, Steafa, Switzerland). The temperature evolution in the lab experiment and in the simulation are shown in Fig. 3(b) as the red and black solid lines, respectively. The two curves show slight differences, which are the result of air turbulences in and around the chamber during the lab experiment. They initially accelerate the temperature raise at the center of the chamber but decelerate the overall heating due to a greater heat dissipation.

For the cooling simulation, the initial chamber temperature is set to 50 °C, and a water stream of 20 °C enters the liquid channels at a flow rate of 30 ml s^{-1}. The sectional views with the temperature contour plots are shown in Fig. 3(d). The chamber is cooled down to 20 °C within 2 min, which is on the same time scale as the heating process. An analogous lab-experiment is carried out in which the 3D printed chamber is preheated to 50 °C before switching to a 20 °C water circuit. The temperature at the center of the chamber is depicted in Fig. 3(c) as black and red solid lines for the simulated and measured data, respectively. The dynamic of the temperature evolution shows a very similar behavior as in the heating curve. Overall, despite the large chamber volume, a stable and quickly switchable temperature control with an elliptical heating and cooling pattern inside the chamber is achieved. A more homogeneous temperature distribution within the chamber is expected when air turbulence is generated, for example, by an external airflow.

We also investigate the homogeneity in heat distribution with respect to a prevention of condensation within the chamber. For that purpose, we generate a water-saturated gas-stream by guiding a dry nitrogen flow at 1.0 l min^{-1} through a washing bottle filled with H_2O and subsequently through a water-heated tube into the chamber. The washing bottle, the gas-stream, and the chamber are heated to both 20 °C and 50 °C for two sets of data. Temperature and humidity are recorded at the center of the chamber with a sensor. After equilibration, the relative humidity (RH) settles at 95 ± 1%RH at 19.8 ± 0.5 °C and at 94 ± 1%RH at 49.5 ± 0.5 °C. No indication of condensation is observed within the chamber. We attribute this on the one hand to the heating of the gas stream, which keeps it at a similar temperature as the chamber, and on the other hand to the advantages of the spherical chamber design with respect to a reduction in water condensation and optimized heat distribution. The offset from 100%RH is partly attributed to the gas stream, which loses 2%–3% in humidity on its way to the chamber and partly to losses within the chamber. However, considering the size and volume of the chamber, which offers good flexibility in experimental options, the high humidity values reached and

the small offset between the humidity at 20 °C and 50 °C indicate an overall homogeneous heat and humidity distribution within the chamber.

An important aspect in neutron scattering experiments is the activation of the sample environment and the generation of background or artifacts on the detector by the sample environment. As the environmental chamber is produced via SLM in a layer-by-layer process, grain boundaries and inhomogeneity are present within the bulk chamber material even though the aluminum alloy powder has been completely melted.[48] For example, previous neutron scattering experiments on 3D printed metals have shown that they produce a strong small-angle scattering signal.[49,50] In addition, the used alloy powder of AlSi10Mg is prone to some impurities of various metals, which must be taken into account with regard to neutron activation and decay times. Thus, it is important to investigate the performance of a printed chamber with a real neutron beam. For this purpose, small-angle neutron scattering (SANS) was performed at the KWS-1 instrument at the FRM II in Garching, Germany.[51] The chamber was placed into the beam path at a distance of 7.78 m from the detector, and its center was aligned to the neutron beam. A monochromatic neutron beam with a wavelength of 4.93 Å and a 10% wavelength spread (FWHM) was used and shaped to a size of 10 × 1 mm^2. Measurements through the chamber windows and through the chamber walls were performed for 20 min each, and the respective 2D scattering data are shown in Figs. 4(a) and 4(b). The measurement through the windows shows that no significant background or secondary scattering from the chamber is detectable. The weak signal in the center can be attributed to statistical fluctuations of the beam around the beam stop. In comparison, the measurement through the walls reveals a strong scattering signal, which is attributed to the grain boundaries within the bulk of the aluminum alloy. The radial scattering pattern reveals an isotropic orientation of the grain boundaries within the AlSi10Mg alloy. The intensity is radially integrated and plotted against the q-values, as shown in Fig. 4(c). From the flat SANS curve, we identify a broad distribution of different grain sizes being present within the 3D printed material. Hence, a strong signal on the detector would be expected if neutrons hit the chamber walls. However, as shown by the window measurement, no signal nor an increase in overall background is detected for a proper chamber alignment.

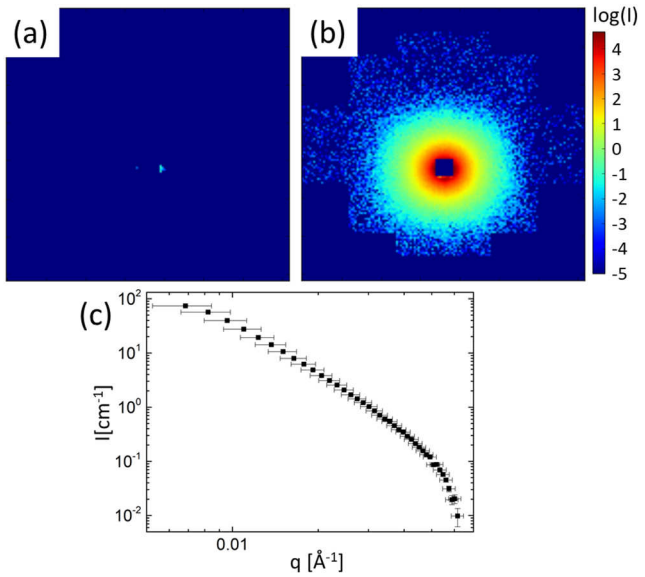

FIG. 4. 2D SANS data of the 3D printed chamber measured (a) through the windows of the chamber and (b) through its walls. (c) Angular integration of the SANS intensity of the wall measurement.

IV. EXAMPLE MEASUREMENTS FOR ToF-NR AND ToF-GISANS

A. Static measurements

To demonstrate the general usability as well as the experimental versatility of the 3D printed environmental chamber, we present two selected static neutron scattering experiments on a poly(styrene-d8-b-methyl methacrylate) (PS-d8-b-PMMA, $M_{w,PS}$ = 55.4 kg mol^{-1} and $M_{w,PMMA}$ = 99.7 kg mol^{-1}) thin film. Diblock copolymer films undergo a micro-phase separation and thereby form characteristic structures with domain distances on the order of tens of nanometers.[52–54] For the given weight average molar masses of the two polymer blocks, the degrees of polymerization are calculated to be N_{PS} = 532 and N_{PMMA} = 996, respectively. Together with the Flory–Huggins interaction parameter χ = 0.043 for PS-b-PMMA at 20 °C, we obtain χN = 66 with $N = N_{PS} + N_{PMMA}$, which is well above the order–disorder transition and is expected to result in a well-ordered structure of the polymer.[55,56] The volume fraction f of the polystyrene block calculates to $f_{PS} = N_{PS}/N$ = 0.35 so that a cylinder morphology can be expected.[57,58] For both the ToF-NR and ToF-GISANS experiments, the chamber is installed at the horizontally oriented reflectometer REFSANS at the FRM II in Garching, Germany.[59] The chamber is connected to a thermal bath (FP50-HL, JULABO Labortechnik GmbH, Seelbach, Germany) and kept at a constant temperature of 20 °C. A humidity and temperature sensor traces the hydrodynamic conditions at a sample height right next to the sample. A 70 × 70 mm^2 silicon wafer has been acid cleaned and plasma treated before a thin layer of PS-d8-b-PMMA dissolved in toluene (ROTISOLV > 99.8%, Carl Roth GmbH + Co. KG, Karlsruhe, Germany) is spin-coated on top (2000 rpm, 60 s). The sample is aligned in height and in lateral position to the center of the chamber. Via spectral reflectance, the film thickness is determined to be 334 nm.

ToF-GISANS proves to be a powerful tool for the structural characterization of thin soft matter samples. In particular, diblock copolymer films give rise to very characteristic scattering features.[60,61] ToF-GISANS measurements are performed under ambient conditions (30%RH and 20.4 °C). The sample–detector distance is 10.33 m, the incident angle is set to 0.5°, and the wavelength band is set to a range from 2 Å to 21 Å with a wavelength resolution of $\Delta\lambda/\lambda$ = 6%. Figure 5(a) shows the 2D scattering data. The 18 images correspond to selected wavelength slices from 2.4 Å to 13.4 Å with a 10% bandwidth around the respective mean wavelength values given in the top left corner of the respective images. As the wavelength increases, the probed reciprocal q-space becomes smaller, which effectively results in a zoom in on the scattering patterns. The last image in the bottom right is a duplicate of the 7.3 Å

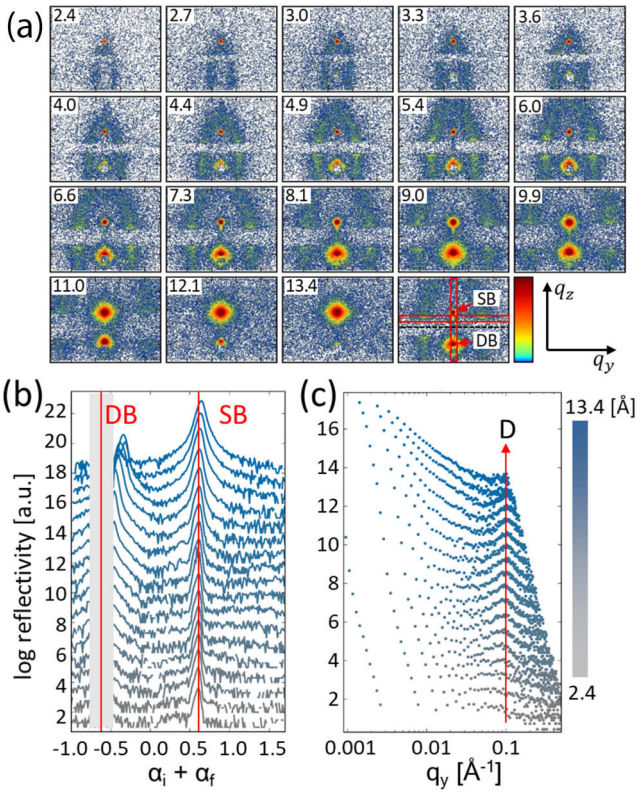

FIG. 5. (a) 2D ToF-GISANS data of the PS-d8-b-PMMA thin film. The 18 images show 10% wavelength slices from 2.4 Å to 13.4 Å with the mean wavelengths denoted in the top left corner of the respective images. The last image in the bottom right depicts a duplicate of the 7.3 Å slice with the direct beam (DB) and the specular beam (SB), as well as the integration box for the vertical cuts (vertical red box) and the horizontal cuts (horizontal red box) indicated. The black dotted line represents the sample horizon. (b) Horizontal line cuts of the 2D ToF-GISANS data for all wavelength slices, starting with the 2.4 Å slice at the bottom, plotted against the sum of incident and exit angles. The positions of the direct beam (DB) and specular beam (SB) are indicated by the red lines. (c) Vertical line cuts of the 2D ToF-GISANS data at the Yoneda peak region for all wavelength slices, starting with the 2.4 Å slice at the bottom, plotted against the horizontal scattering vector component q_y. The feature around 0.1 Å corresponds to the characteristic micro-phase separation structure of the deuterated PS block in the PMMA matrix and is marked by the red arrow as D.

slice and indicates the positions of the direct beam (DB) and the specular beam (SB) of the neutron beam on the detector image. The black dotted line is the sample horizon, and the vertical and horizontal red boxes correspond to the vertical and the horizontal cut regions, respectively. The 2D ToF-GISANS data show that the film structure is well resolved. The micro-phase separation structure is defect-rich, and thus instead of characteristic sharp Bragg peaks, a ring-shaped intensity of the Bragg signal is found around the DB and the SB.[60] With respect to the overall statistics on the detector, the signal to noise ratio is not lower compared to previous measurements without the 3D printed chamber, proving that secondary scattering from the chamber does not pose a problem with regard to background generation.[62,63] Vertical line cuts of all 18 wavelength slices are shown in Fig. 5(b) with increasing mean wavelength from bottom to top. The positions of the direct and specular beam are marked by the red lines. Horizontal line cuts are performed at the Yoneda region, which marks scattering under the material specific critical angle $\alpha_c = \lambda(_{SLD}/\pi)^{0.5}$ defined by the scattering length density (SLD) of the material. The cuts are shown in Fig. 5(c) for increasing mean wavelength from bottom to top. The probed q_y-range changes due to the different wavelengths, but the Bragg peak arising from the micro-phase separation of the polymer remains constant at around 0.1 Å^{-1}, which corresponds to a structure size of about 14 nm. For a more detailed analysis, the curves are modeled based on the distorted wave Born approximation (DWBA) and the effective interface approximation (EIA) using spherical form factors distributed on a 1D paracrystal lattice.[64,65] The extracted form and structure factor are determined to be (14 ± 1) nm and (58 ± 4) nm, respectively, and correspond to the PS domain size and its average inter-domain distance within the PMMA matrix. Overall, the spherical environmental chamber is well suited for ToF-GISANS measurements and provides reliable scattering data at defined environmental conditions with no significant background contribution from the 3D printed material nor any detectable activation right after the end of the experiment.

As a second experiment, ToF-NR is performed on the very same sample at room temperature and under 0% humidity conditions using a dry nitrogen gas stream. NR is known to be able to resolve the SLD profile along the surface normal with sub-nm precision.[66,67] The sample detector distance is 9.58 m, and the wavelength band is set to 3 Å–21 Å with a wavelength resolution of $\Delta\lambda/\lambda = 1.5\%$. The beam is collimated to a width of 60 mm and a height of 0.2 mm. The reflected intensity is recorded under an incident angle of 0.6° for 20 min and 2.4° for 100 min in order to cover a larger q-range. Prior to the ToF-NR measurements, the direct beam has been measured for all used instrument settings to get the reflectivity values. These also confirm that no background from the chamber is visible on the detector when comparing them to direct beam measurements through air. Figure 6(a) shows the superimposed reflectivity curve of both measurements in the q-region from 0.01 Å^{-1} to 0.2 Å^{-1}. The curve is a combination of a large fringe spacing of around 0.05 Å^{-1} and a small fringe spacing of around 0.002 Å^{-1} visible in the low q-region [see the inset of Fig. 6(a)], identifying a multilayer system within the thin polymer film. In order to obtain the values for film thickness and SLD, the collected data are fitted using the MOTOfit plugin for IGOR Pro v6.37 by Nelson.[68] The extracted values are depicted graphically in Fig. 6(b), showing the SLD profile of the film with the silicon substrate at the bottom and the polymer film on top (the black dotted line marks the substrate boundary). At the substrate boundary, the polymer film reveals a stack of layers with alternating high and low SLD values, which is accounted for the diblock copolymer film being layered parallel to the substrate surface (SLD values of PS-d8 = 6.06×10^{-6} Å^{-2} and of PMMA = 1.06×10^{-6} Å^{-2}). The polymer film has an average SLD of 2.97×10^{-6} Å^{-2} and a total film thickness of 322.3 nm, which is in good agreement with the data obtained from the spectral reflectance measurement. The measurement shows a clean reflectivity curve with usual background, showing that even for broad beams and larger angles, the chamber produces little to no additional background on the detector.

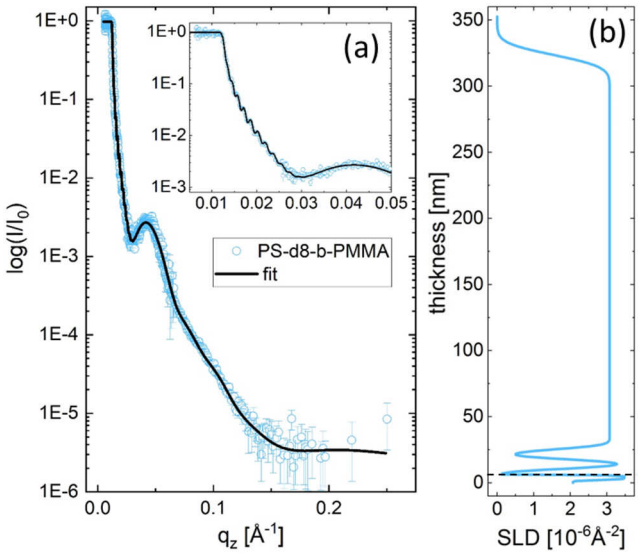

FIG. 6. (a) ToF-NR reflectivity curve of a PS-d8-b-PMMA thin film. The inset is the zoomed-in view of the low q_z-region to highlight the additional curve modulation arising from the film thickness (322.3 nm). The black line is the model fit to the scattering data. (b) Vertical SLD profile of the polymer film. The black dotted line marks the boundary between the silicon substrate and the diblock copolymer film.

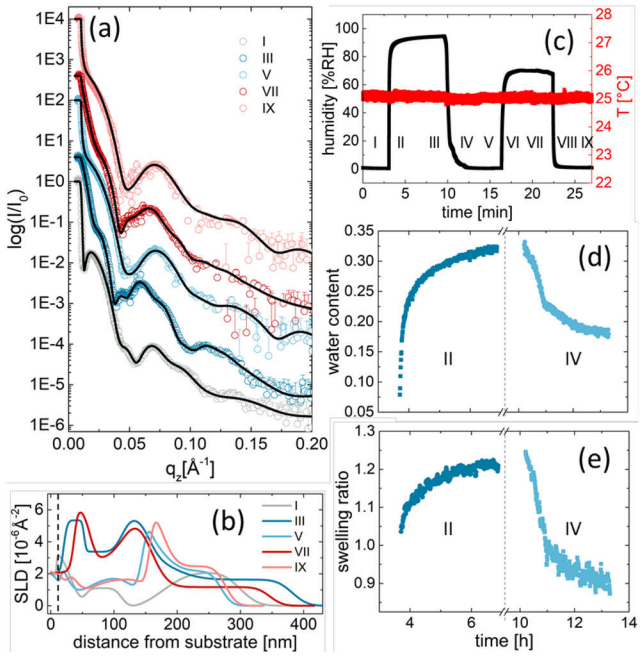

FIG. 7. (a) ToF-NR reflectivity curves of the dry static states (I), (V), and (IX) and the swollen static states (III) and (VII) of a cyclic swelling and drying experiment [as shown in (c)] of a PNIPAM microgel thin film. (b) SLD profiles extracted from the reflectivity data plotted against the distance from the silicon substrate. The polymer–substrate interface is marked by the black dotted line. (c) Relative humidity (black) and temperature (red) measured over the course of two subsequent swelling and drying cycles. The respective states (I) to (IX) are indicated. Evolution of (d) water content and (e) film thickness during the first swelling (II) and the first drying (IV) process.

B. Kinetic measurements

We also perform kinetic ToF-NR measurements under changing humidity conditions to demonstrate the stable temperature control within the chamber as well as the thereby achieved accurate adjustment of the relative humidity. For that purpose, we use a thin microgel film of poly(N-isopropylacrylamide) (PNIPAM) cross-linked with N,N′-methylenebisacrylamide (BIS) (2.5 mol PNIPAM: 1 mol BIS) with a thin aluminum metal layer evaporated on top. The preparation routine of the polymer film follows the same steps, as described in our previous work.[28] The aluminum layer, which can enable potential use of such microgel thin films as humidity sensors, is deposited in a thermal evaporation chamber with a pre-calibrated thickness of around 10 nm. We measure two cycles of hydration and drying of the film. The related sample states are denoted as (I) dry static state 1, (II) swelling kinetic state 1, (III) swollen static state 1, (IV) drying kinetic state 1, (V) dried static state 2, (VI) swelling kinetic state 2, (VII) swollen static state 2, (VIII) drying kinetic state 2, and a (IX) dried static state 3. The chamber humidity is supplied via a gas stream that is mixed from a saturated gas-flow of dry nitrogen led through a washing bottle filled with D_2O and a second pure dry nitrogen gas stream. For the first cycle, a water-saturated gas stream is used, while for the second cycle, we mix 70% of the saturated gas stream with 30% of the pure dry nitrogen gas stream. The measurements are carried out at the REFSANS instrument at a temperature of 25 °C using the same settings for static measurements as described before. Kinetic measurements are recorded for 180 min with a time resolution of 30 s at an incident angle of 0.76°.

The ToF-NR reflectivity data of the static film states (I), (III), (V), (VII), and (IX) are shown in Fig. 7(a) together with the respective SLD profiles in Fig. 7(b). The evolution of the temperature and humidity is depicted in Fig. 7(c). In the first cycle, we reach 95%RH, and in the second cycle, we reach 70%RH. The three dry states all equilibrate at around 0%RH. During the entire experiment, the temperature remains stable at 25 ± 0.5 °C. The values for film thickness and film SLD are extracted via best model fits and are graphically represented in the SLD profiles in Fig. 7(b). The top layer of around 15 nm represents a metal/polymer intermixing layer, whereas the layers below are assumed to be the pristine polymer. The profiles reveal D_2O enrichment layers at the polymer–substrate and polymer–metal interfaces, respectively. It also shows that the swelling process mainly happens within the top intermixing layer of the metal and polymer. The exact processes during the swelling and drying are extracted from the kinetic data recorded every 30 s. Selected ToF-NR reflectivity curves and the corresponding fits are shown for all four kinetics in Fig. S1 of the supplementary material. From the fits, we extract an SLD and film thickness, which we transform into a water content Φ and a swelling ratio (SR), as described in the supplementary material. The Φ and SR plots are shown for the first cycle in Figs. 7(d) and 7(e) and for the second cycle in Figs. S2(a) and S2(b) of the supplementary material, respectively. During the first cycle, the film reaches Φ values of 35% and a SR of 1.2, while during the second cycle, it reaches Φ values of 28% and a SR of 1.1. The smaller film thicknesses after the second and third drying

process compared to the films initial state are accounted for rearrangements, which typically happen within the as prepared polymer film during a swelling process. In comparison, we reach the same dry thicknesses at the start and end of the second cycle, highlighting the good control achieved with the chamber. The differences between the extracted water content and swelling ratios are explained in more detail in our previous work on similar polymer thin films and are related to a deuteration of the polymer in the presence of D_2O.[28] Overall, these experiments showcase the stability and adjustability of the temperature and relative humidity within the chamber, which makes it a reliable sample environment for investigations relating to relative humidity.

V. CONCLUSION

We designed, manufactured, and tested an environmental chamber for ToF-NR and ToF-GISANS experiments using state-of-the-art 3D metal-printing technology. Key features of the chamber are its spherical design, which helps to reduce heat gradients within the chamber and is also of high interest for high humidity experiments, the fluidic channels within its walls for heating and cooling the sample from all directions, and its large volume, which allows for a high degree of flexibility with regard to the sample size and the installation of complementary measurement equipment. Temperature simulations and laboratory experiments have shown that the temperature can be switched within a few minutes. Test measurements of the 3D printed material have revealed that the grain boundaries within the chamber material produce a strong, but spatially uniform, scattering signal. Furthermore, it has been proven that under correct beam alignment, no secondary scattering or other additional background is produced by the chamber. Exemplary ToF-GISANS and ToF-NR measurements on a thin 70 × 70 mm^2 deuterated diblock-copolymer thin film (PS-d8-b-PMMA) are provided as example experiments. They allowed a thorough investigation of the film structure and composition and did not reveal any detrimental influence of the chamber compared to previous experiments performed on the same instrument. Additional ToF-NR measurements under varying humidity conditions are shown to prove the chambers viability on a real sample system and to further demonstrate its stability and control over temperature and humidity.

Conclusively, additive manufacturing methods can be used very well for neutron sample environment fabrication where a flexible design is required. Moreover, it is expected that the spherical environmental chamber will provide a flexible environment for a multitude of future NR and GISANS experiments.

SUPPLEMENTARY MATERIAL

See the supplementary material for selected ToF-NR reflectivity curves of the swelling and drying kinetics of a PNIPAM microgel thin film, temporal evolution of the water content and swelling ratio, and calculation of swelling ratio and water content with the respective SLD values.

ACKNOWLEDGMENTS

The authors thank the German Ministry for Education and Research (BMBF) for funding within the project "FlexiProb" (Grant No. 05K2016) and for financial support. This work was based upon experiments performed at the instrument REFSANS operated by HZG and the instrument KWS-1 operated by JCNS at the Heinz Maier-Leibnitz Zentrum (MLZ), Garching, Germany. We acknowledge beamtime allocation, excellent equipment, and support. We thank PROTIQ GmbH for their technical assistance and for printing the final design of the environmental chamber and I. Ehring and T. Hellweg for providing the PNIPAM microgel.

DATA AVAILABILITY

Raw data were generated at the Heinz Maier-Leibnitz Zentrum (MLZ, Garching, Germany) large scale facility. The data that support the findings of this study are available from the corresponding author upon reasonable request.

REFERENCES

[1] V. F. Sears, Neutron News **3**, 26 (2006).
[2] J. S. Higgins and H. C. Benoit, *Polymers and Neutron Scattering* (Clarendon Press, Oxford, 2009), reprinted (with corr.) [2. Nachdr.].
[3] See https://www.ncnr.nist.gov/resources/activation/ for the SLD calculation via the material density.
[4] T. P. Russell, Mater. Sci. Rep. **5**, 171 (1990).
[5] J. Penfold and R. K. Thomas, J. Phys.: Condens. Matter **2**, 1369 (1990).
[6] C. F. Majkrzak and G. P. Felcher, MRS Bull. **15**, 65 (1990).
[7] P. Müller-Buschbaum, J. S. Gutmann, and M. Stamm, Phys. Chem. Chem. Phys. **1**, 3857 (1999).
[8] P. Müller-Buschbaum, J. S. Gutmann, R. Cubitt, and M. Stamm, Colloid Polym. Sci. **277**, 1193 (1999).
[9] J. Kraus, P. Müller-Buschbaum, T. Kuhlmann, D. W. Schubert, and M. Stamm, Europhys. Lett. **49**, 210 (2000).
[10] P. Müller-Buschbaum, Polym. J. **45**, 34 (2013).
[11] J. W. Kiel, M. E. Mackay, B. J. Kirby, B. B. Maranville, and C. F. Majkrzak, J. Chem. Phys. **133**, 074902 (2010).
[12] H. Chen, R. Hegde, J. Browning, and M. D. Dadmun, Phys. Chem. Chem. Phys. **14**, 5635 (2012).
[13] A. J. Clulow, C. Tao, K. H. Lee, M. Velusamy, J. A. McEwan, P. E. Shaw, N. L. Yamada, M. James, P. L. Burn, I. R. Gentle, and P. Meredith, Langmuir **30**, 11474 (2014).
[14] J. W. Kingsley, P. P. Marchisio, H. Yi, A. Iraqi, C. J. Kinane, S. Langridge, R. L. Thompson, A. J. Cadby, A. J. Pearson, D. G. Lidzey, R. A. L. Jones, and A. J. Parnell, Sci. Rep. **4**, 5286 (2014).
[15] L. Bießmann, L. P. Kreuzer, T. Widmann, N. Hohn, J.-F. Moulin, and P. Müller-Buschbaum, ACS Appl. Mater. Interfaces **10**, 9865 (2018).
[16] B. Jerliu, L. Dörrer, E. Hüger, G. Borchardt, R. Steitz, U. Geckle, V. Oberst, M. Bruns, O. Schneider, and H. Schmidt, Phys. Chem. Chem. Phys. **15**, 7777 (2013).
[17] S. Ohisa, G. Matsuba, N. L. Yamada, Y.-J. Pu, H. Sasabe, and J. Kido, Adv. Mater. Interfaces **1**, 1400097 (2014).
[18] J. A. McEwan, A. J. Clulow, P. E. Shaw, A. Nelson, T. A. Darwish, P. L. Burn, and I. R. Gentle, Adv. Mater. Interfaces **3**, 1600184 (2016).
[19] S. Ueda, S. Koizumi, A. Ohira, S. Kuroda, and H. Frielinghaus, Physica B **551**, 309 (2018).
[20] H. Cavaye, A. R. G. Smith, M. James, A. Nelson, P. L. Burn, I. R. Gentle, S.-C. Lo, and P. Meredith, Langmuir **25**, 12800 (2009).
[21] A. Junghans, E. B. Watkins, R. D. Barker, S. Singh, M. J. Waltman, H. L. Smith, L. Pocivavsek, and J. Majewski, Biointerphases **10**, 019014 (2015).
[22] R. Simič, M. Kalin, T. Hirayama, P. Korelis, and T. Geue, Tribol. Lett. **53**, 199 (2014).
[23] K. Theis-Bröhl, D. Mishra, B. P. Toperverg, H. Zabel, B. Vogel, A. Regtmeier, and A. Hütten, J. Appl. Phys. **110**, 102207 (2011).

[24]F. Cousin, J. Jestin, G. Chaboussant, S. Gautrot, A. Menelle, and F. Ott, Eur. Phys. J. Spec. Top. **167**, 177 (2009).
[25]M. Wolff, A. Magerl, and H. Zabel, Physica B **357**, 84 (2005).
[26]F. Lipfert, H. Frielinghaus, O. Holderer, S. Mattauch, M. Monkenbusch, N. Arend, and D. Richter, Phys. Rev. E **89**, 042303 (2014).
[27]G. E. Newby, E. B. Watkins, D. H. Merino, P. A. Staniec, and O. Bikondoa, RSC Adv. **5**, 104164 (2015).
[28]T. Widmann, L. P. Kreuzer, N. Hohn, L. Bießmann, K. Wang, S. Rinner, J.-F. Moulin, A. J. Schmid, Y. Hannappel, O. Wrede, M. Kühnhammer, T. Hellweg, R. von Klitzing, and P. Müller-Buschbaum, Langmuir **35**, 16341 (2019).
[29]L. P. Kreuzer, T. Widmann, L. Bießmann, N. Hohn, J. Pantle, R. Märkl, J.-F. Moulin, V. Hildebrand, A. Laschewsky, C. M. Papadakis, and P. Müller-Buschbaum, Macromolecules **53**, 2841 (2020).
[30]I. F. Bailey, Z. Kristallogr. **218**, 77 (2003).
[31]J. Gonthier, M. A. Barrett, O. Aguettaz, S. Baudoin, E. Bourgeat-Lami, B. Demé, N. Grimm, T. Hauß, K. Kiefer, E. Lelièvre-Berna, A. Perkins, and D. Wallacher, J. Neutron Res. **21**, 65 (2019).
[32]D. La Salas-de Cruz, J. G. Denis, M. D. Griffith, D. R. King, P. A. Heiney, and K. I. Winey, Rev. Sci. Instrum. **83**, 025112 (2012).
[33]T. A. Harroun, H. Fritzsche, M. J. Watson, K. G. Yager, O. M. Tanchak, C. J. Barrett, and J. Katsaras, Rev. Sci. Instrum. **76**, 065101 (2005).
[34]S. H. Huang, P. Liu, A. Mokasdar, and L. Hou, Int. J. Adv. Manuf. Technol. **67**, 1191 (2013).
[35]K. V. Wong and A. Hernandez, ISRN Mech. Eng. **2012**, 1.
[36]A. Olsson and A. R. Rennie, J. Appl. Crystallogr. **49**, 696 (2016).
[37]S. Woosley, N. Abuali Galehdari, A. Kelkar, and S. Aravamudhan, J. Mater. Res. **33**, 3657 (2018).
[38]W. E. Frazier, J. Mater. Eng. Perform. **23**, 1917 (2014).
[39]P. Müller-Buschbaum, Eur. Polym. J. **81**, 470 (2016).
[40]D. Magerl, M. Philipp, X.-P. Qiu, F. M. Winnik, and P. Müller-Buschbaum, Macromolecules **48**, 3104 (2015).
[41]L. Bießmann, N. Saxena, N. Hohn, M. A. Hossain, J. G. C. Veinot, and P. Müller-Buschbaum, Adv. Electron. Mater. **5**, 1800654 (2019).
[42]S. Guo, B. Cao, W. Wang, J.-F. Moulin, and P. Müller-Buschbaum, ACS Appl. Mater. Interfaces **7**, 4641 (2015).
[43]K. S. Narayan and N. Kumar, Appl. Phys. Lett. **79**, 1891 (2001).
[44]L. P. Kreuzer, T. Widmann, N. Hohn, K. Wang, L. Bießmann, L. Peis, J.-F. Moulin, V. Hildebrand, A. Laschewsky, C. M. Papadakis, and P. Müller-Buschbaum, Macromolecules **52**, 3486 (2019).
[45]M.-G. Medici, A. Mongruel, L. Royon, and D. Beysens, Phys. Rev. E **90**, 062403 (2014).
[46]H-5800-1084-01-A_AlSi10Mg-0403_200_W_material_data_sheet.
[47]N. Takata, H. Kodaira, K. Sekizawa, A. Suzuki, and M. Kobashi, Mater. Sci. Eng., A **704**, 218 (2017).
[48]J. Wu, X. Q. Wang, W. Wang, M. M. Attallah, and M. H. Loretto, Acta Mater. **117**, 311 (2016).
[49]C. A. Brice, W. A. Tayon, J. A. Newman, M. V. Kral, C. Bishop, and A. Sokolova, Mater. Charact. **143**, 50 (2018).
[50]M. Calvo-Dahlborg, P. S. Popel, M. J. Kramer, M. Besser, J. R. Morris, and U. Dahlborg, J. Alloys Compd. **550**, 9 (2013).
[51]H. Frielinghaus, A. Feoktystov, I. Berts, and G. Mangiapia, JLSRF **1**, A28 (2015).
[52]M. J. Fasolka and A. M. Mayes, Annu. Rev. Mater. Res. **31**, 323 (2001).
[53]I. W. Hamley, Nanotechnology **14**, R39–R54 (2003).
[54]M. Li, C. A. Coenjarts, and C. K. Ober, in *Block Copolymers II*, edited by V. Abetz (Springer-Verlag, Berlin, Heidelberg, 2005), Vol. 190, p. 183.
[55]Y. Zhao, E. Sivaniah, and T. Hashimoto, Macromolecules **41**, 9948 (2008).
[56]L. Leibler, Macromolecules **13**, 1602 (1980).
[57]J.-Y. Wang, W. Chen, C. Roy, J. D. Sievert, and T. P. Russell, Macromolecules **41**, 963 (2008).
[58]H. Feng, X. Lu, W. Wang, N.-G. Kang, and J. W. Mays, Polymers **9**, 494 (2017).
[59]J.-F. Moulin and M. Haese, JLSRF **1**, A9 (2015).
[60]P. Müller-Buschbaum, G. Kaune, M. Haese-Seiller, and J.-F. Moulin, J. Appl. Crystallogr. **47**, 1228 (2014).
[61]P. Busch, M. Rauscher, J.-F. Moulin, and P. Müller-Buschbaum, J. Appl. Crystallogr. **44**, 370 (2011).
[62]R. S. Märkl, N. Hohn, E. Hupf, L. Bießmann, V. Körstgens, L. P. Kreuzer, G. Mangiapia, M. Pomm, A. Kriele, E. Rivard, and P. Müller-Buschbaum, IUCrJ **7**, 268 (2020).
[63]G. Kaune, M. Haese-Seiller, R. Kampmann, J.-F. Moulin, Q. Zhong, and P. Müller-Buschbaum, J. Polym. Sci., Part B: Polym. Phys. **48**, 1628 (2010).
[64]G. Renaud, R. Lazzari, and F. Leroy, Surf. Sci. Rep. **64**, 255 (2009).
[65]P. Müller-Buschbaum, in *Polymer Surfaces and Interfaces*, edited by M. Stamm (Springer Berlin Heidelberg, Berlin, Heidelberg, 2008), p. 17.
[66]D. G. Bucknall, S. A. Butler, and J. S. Higgins, J. Phys. Chem. Solids **60**, 1273 (1999).
[67]J. Penfold, Curr. Opin. Colloid Interface Sci. **7**, 139 (2002).
[68]A. Nelson, J. Appl. Crystallogr. **39**, 273 (2006).